

Article

Effect of Thickness on Ferroelectric Properties of $\text{Bi}_{3.25}\text{La}_{0.75}\text{Ti}_3\text{O}_{12}$ Thin Films

Wenfeng Yue¹, Yali Cai², Quansheng Guo², Dawei Wang^{1,*}  and Tingting Jia^{2,*} ¹ School of Instrumentation Science and Engineering, Harbin Institute of Technology, Harbin 150001, China² School of Materials Science and Engineering, Hubei University, Wuhan 430062, China

* Correspondence: wangdawei102@gmail.com (D.W.); jia.tingting@hubei.edu.cn (T.J.)

Abstract: The pursuit of low-power/low-voltage operation in devices has prompted a keen interest in the mesoscale effects within ferroelectric thin films. The downsizing of ferroelectrics can significantly influence performance; for instance, the remanent polarization and coercive field are susceptible to alterations based on thickness. In this study, randomly oriented $\text{Bi}_{3.25}\text{La}_{0.75}\text{Ti}_3\text{O}_{12}$ thin films were fabricated on Pt/Ti/SiO₂/Si substrates using the sol-gel method, and SEM observations revealed rod-like grains in all thin films. The investigation delved into the correlation between dielectric and ferroelectric properties with thin film thickness. The thin film exhibited an increased remanent polarization and a reduced coercive electric field. Additionally, the ferroelectric domain structure was scrutinized through PFM, and the resistor properties of the BLT4 thin film were studied, which shows the potential of BLT thin films in non-volatile memory and memristor.

Keywords: ferroelectric; $\text{Bi}_{3.25}\text{La}_{0.75}\text{Ti}_3\text{O}_{12}$; thickness; thin films

1. Introduction

Ferroelectric thin films exhibit diverse properties, such as ferroelectricity, piezoelectricity, dielectricity, pyroelectricity, and photoelectric effects, rendering them suitable for various applications including ferroelectric memory, piezoelectric drivers, infrared detectors, and optoelectronic devices [1–5]. Traditional ferroelectric materials, predominantly lead-based compounds, are exemplified by the widely used lead zirconate titanate (PZT) in commercial applications due to their robust ferroelectric and piezoelectric characteristics [6,7]. However, the environmental and health concerns arising from the volatilization of lead in lead-based materials necessitate the exploration of lead-free alternatives. Bismuth-based titanate and bismuth ferrite emerge as promising candidates for lead-free piezoelectric materials. Notably, bismuth titanate ($\text{Bi}_4\text{Ti}_3\text{O}_{12}$, BIT) exhibits favorable properties, including a small coercive field, a low leakage current density, excellent fatigue resistance, and applicability in non-volatile memory [8–10].

BIT, classified as a typical three-layer bismuth layered ferroelectric (BLSF) material, consists of a bismuth oxide layer (Bi_2O_3)²⁺ and a perovskite-like layer ($\text{A}_{n-1}\text{B}_n\text{O}_{3n+1}$)²⁻ along the c-axis direction [11,12]. Characterized by strong anisotropy, BIT demonstrates spontaneous polarization of approximately 50 $\mu\text{C}/\text{cm}^2$ along the a-axis and 4 $\mu\text{C}/\text{cm}^2$ along the c-axis. Additionally, it features a low film deposition temperature and a high Curie temperature ($T_c = 675^\circ\text{C}$) [13,14]. Despite its favorable properties, BIT faces challenges such as instability in the oxidation state of Ti ions and volatility in Bi ions during the sintering process. These issues lead to defects, resulting in a high leakage current and domain pinning, thereby affecting its practical applications [9,15]. To enhance its ferroelectric properties, researchers have explored the substitution of Bi^{3+} ions in the perovskite-like layer ($\text{Bi}_2\text{Ti}_3\text{O}_{12}$)²⁺ with trivalent rare-earth ions such as Pr^{3+} , Nd^{3+} , Sm^{3+} , Eu^{3+} , and La^{3+} [1,16–19]. In 1999, Park et al. reported a ferroelectric thin film of La-doped BIT, $\text{Bi}_{3.25}\text{La}_{0.75}\text{Ti}_3\text{O}_{12}$ (BLT) [11]. Wu et al. demonstrated that the application of tensile or compressive stress on the surface of BLT thin films in the high-field region (>75 kV/cm)



Citation: Yue, W.; Cai, Y.; Guo, Q.; Wang, D.; Jia, T. Effect of Thickness on Ferroelectric Properties of $\text{Bi}_{3.25}\text{La}_{0.75}\text{Ti}_3\text{O}_{12}$ Thin Films. *Ceramics* **2024**, *7*, 29–38. <https://doi.org/10.3390/ceramics7010003>

Academic Editor: Gilbert Fantozzi

Received: 10 November 2023

Revised: 30 December 2023

Accepted: 4 January 2024

Published: 6 January 2024



Copyright: © 2024 by the authors. Licensee MDPI, Basel, Switzerland. This article is an open access article distributed under the terms and conditions of the Creative Commons Attribution (CC BY) license (<https://creativecommons.org/licenses/by/4.0/>).

effectively mitigates the leakage current [20]. Furthermore, substituting high-valent cations for Ti^{4+} at the B site proves instrumental in eliminating oxygen vacancy defects, thereby enhancing remanent polarization and reducing the leakage current. BIT thin films co-doped with Sm and Ta, denoted as BSTTO, exhibited markedly improved ferroelectric properties, boasting a higher remanent polarization ($2P_r = 46.2 \mu\text{C}/\text{cm}^2$) compared to BIT thin films ($2P_r = 26 \mu\text{C}/\text{cm}^2$) [21]. Various techniques, including pulsed laser deposition (PLD) [22], magnetron sputtering (MS) [23], metal–organic chemical vapor deposition (MOCVD) [24], and the sol–gel method [25], have been employed for the preparation of BLT ferroelectric thin films. Among these, the sol–gel process stands out for its cost-effectiveness, facile stoichiometry control, and uniform deposition over large areas, making it versatile for widespread applications. Notably, factors such as the precursor solution, annealing conditions, film thickness, and substrate properties exert substantial influence on film orientation [25–27]. Optimal film layer thicknesses of 30, 50, and 100 nm corresponded to preferentially oriented thin films with (001), (100), and (117) orientations, respectively [28]. By adjusting the grain size of BLT through annealing temperature modulation, Yang et al. achieved a higher energy storage density, rendering BLT ferroelectric thin films suitable for high-energy-density storage devices, thereby expanding their application scope [29]. In addition, information storage technology stands as one of the most rapidly advancing fields within the realm of integrated circuits. Among its components, memory stands as the pivotal core in information storage technology. However, conventional storage devices have reached a point where they can no longer meet the burgeoning demands of information storage technology. Consequently, the pursuit of developing a new generation of memristors has captured academic interest in recent years. The development of ferroelectric materials with resistive switching characteristics holds significant importance for memristors.

In this study, lead-free BLT thin films were synthesized using the sol–gel method, and the adjustment of spin coating times yielded BLT thin films with exceptional ferroelectric properties. The dielectric and ferroelectric characteristics of thin films subjected to varying spin coating times were systematically compared across different electric field strengths and frequencies. The microscopic ferroelectricity of the BLT film and the microscopic evolution of the domain wall of the BLT film were studied through PFM observation. The resistor characteristics of the BLT4 thin film were studied, demonstrating its potential application in memristor.

2. Materials and Methods

The $\text{Bi}_{3.25}\text{La}_{0.75}\text{Ti}_3\text{O}_{12}$ thin films were fabricated using the sol–gel method on Pt/Ti/SiO₂/Si substrates. The precursor solution was composed of bismuth(III) acetate (Aladdin, Shanghai, China), lanthanum(III) acetate (Aladdin, Shanghai, China), and tetrabutyl titanate (Aladdin, Shanghai, China) as primary raw materials, with propionic acid (Aladdin, Shanghai, China) as the solvent and ethanolamine (Aladdin, Shanghai, China) as the stabilizer. The quantities of bismuth acetate, lanthanum acetate, and tetrabutyl titanate were determined according to stoichiometric proportions, with an additional 5% of bismuth acetate to compensate for Bi volatilization during annealing. The synthesis process entailed the gradual addition of bismuth acetate and lanthanum acetate to propionic acid, followed by stirring at room temperature until complete dissolution. Subsequently, tetrabutyl titanate was introduced, and a specific amount of ethanolamine was added to stabilize the colloid. The mixture was stirred at room temperature for one day to yield a yellow stock solution, and the concentration of precursor solution was 0.10 mol/L. This solution was spun at 6000 rpm for 20 s and then pyrolyzed on a hot stage (C-MAG HS 7, IKA, Staufen, Germany) at 400 °C for 5 min. This procedure was iterated four, five, six, and seven times to produce the samples denoted as BLT4, BLT5, BLT6, and BLT7, respectively. Finally, the samples underwent annealing in an infrared annealing furnace (IRLA-1200, Wuhan JouleYacht Technology Co., LTD, Wuhan, China) at 700 °C in an air atmosphere for 30 min.

The thin films' phase analysis and crystallographic orientation were determined using X-ray diffraction (XRD, D8 Advance X, Bruker, Germany) with $\text{CuK}\alpha$ radiation at room temperature. Surface topography and cross-section were examined using a scanning electron microscope (SEM, Apreo 2, Thermo Scientific, Waltham, MA, USA). The piezoelectric response and domain structure of the BLT thin films were characterized using piezoelectric force microscopy (AFM/PFM, Cypher S, Oxford Instruments, Abingdon, Oxfordshire, UK). Before electrical characterization, Au top electrodes with a 0.5 mm diameter were deposited onto the thin films through magnetron sputtering (ETD-800, Vision Precision Instruments, Beijing, China), forming Au/BLT/Pt capacitors. The hysteresis loop, leakage current characteristic, and current–voltage loop were characterized using a ferroelectric analyzer (Precision Multiferroic II, Radiant, Albuquerque, NM, USA), and the dielectric constant and dielectric loss were determined using an impedance analyzer (WK6500B, Wayne Kerr, Woburn, Massachusetts, UK). The resistor characteristics (I-V curve) of the device were tested using a semiconductor analyzer (4200A-SCS, Keithley, Seattle, WA, USA).

3. Results and Discussion

Figure 1 depicts the X-ray diffraction (XRD) patterns of BLT thin films deposited on (111)Pt/Ti/SiO₂/Si substrates. The thin films exhibit complete crystallization and demonstrate polycrystalline structures (ICDD/PDF No. 00-035-2795), with no observable secondary phases in the XRD scans. Based on the intensity of the (117) XRD reflection, the following formula [28] can be used to estimate the degree of preferred orientation of BLT films:

$$\alpha_{117} = \frac{I(117)}{I(008) + I(117) + I(200)} \quad (1)$$

where $I(006)$, $I(117)$, and $I(200)$ stand for the integrated peak intensities for (008), (117), and (200) diffraction lines, respectively. α_{117} would be about 66% in a fully random film. This indicates that all of the thin films possessed random orientation. Increasing the number of spin coating cycles leads to a significant enhancement in the intensities of (111), (220), (1115), and (317) peaks relative to the background noise level. This is to be expected as a consequence of the film thickness increase with the number of spun layers. The slight decrease in α_{117} with the number of spin cycles is probably due to this increase in the intensities of the weak (008) and (200/020) lines relative to the background noise in the XRD scans, rather than any change in preferred orientation.

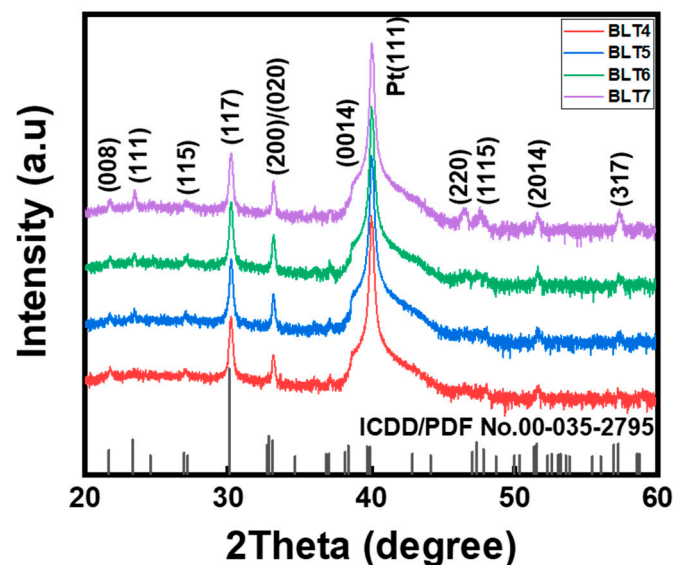


Figure 1. XRD patterns of BLT4, BLT5, BLT6, and BLT7 thin films.

In Figure 2, surface images of the BLT thin films on Pt/Ti/SiO₂/Si substrates with varying spin coating cycles are presented. The micrographs reveal dense and smooth

thin films without discernible cracks or bubbles, which indicates that all of the thin films have good quality. With an increasing number of spin coatings, the BLT grains exhibit elongation, which is confirmed by SEM micrographs. The thin films primarily consist of rod-like grains oriented with different lengths. It is not clear whether these grains are rods or plates, which are viewed edge-on. The formation of rod-like grains can be attributed to the anisotropic growth of the BIT-based material, driven by lower c-plane interface energy compared to the a/b surface, resulting in faster growth in the plane perpendicular to the crystallographic c-axis [28]. In the process of film preparation, the shapes of grains depend on nucleation and grain growth. According to Schwartz's theory, in films with interface nucleation, the grains are columnar, while in films with interface and bulk nucleation, the grains are fine [30]. Therefore, it is speculated that when the film thickness is low, interface nucleation is predominant, and as the thickness gradually increases, it transitions to both interface and bulk nucleation. Furthermore, the grain density is influenced by nucleation centers and the surface migration of adsorbed atoms. With an increase in the number of spin-coating layers, i.e., an increase in thickness, the surface diffusion of adsorbed atoms is restricted, and the density of nucleation centers increases, resulting in a more uniform distribution of particle aggregation, and as the width of the rod increases, it is easier for them to make contact with each other, which also leads to the smaller width of the grain during the growth process [31]. The cross-sectional images in Figure 2e–h depict thin films with varying layer counts. The thicknesses for four, five, six, and seven layers are 140 nm, 180 nm, 210 nm, and 240 nm, respectively, with each layer measuring approximately 35 nm.

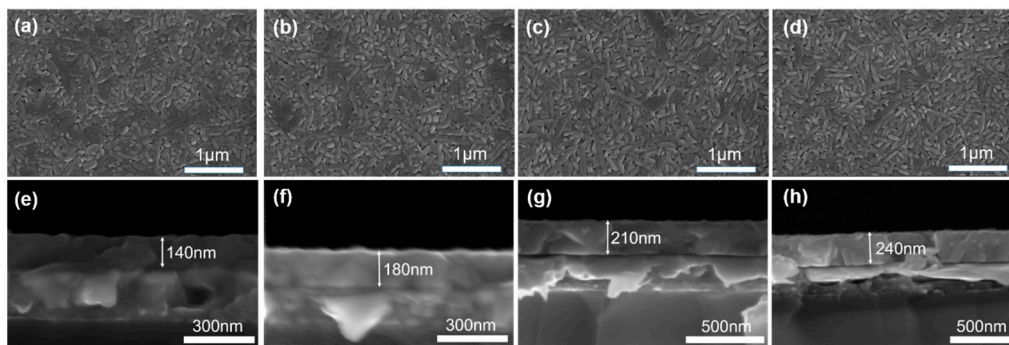


Figure 2. SEM micrographs and cross-sections of $\text{Bi}_{3.25}\text{La}_{0.75}\text{Ti}_4\text{O}_{12}$ thin films; (a,e) BLT4, (b,f) BLT5, (c,g) BLT6, (d,h) BLT7.

The polarization–voltage hysteresis loop was measured at 1 kHz for each thin film sample, and the remanent polarization (P_r) was extracted from the hysteresis loop. The hysteresis loops for BLT thin films with different thicknesses are presented in Figure 3a, and the corresponding thickness-dependent P_r values are illustrated. It was observed that as the number of spin coatings increased, P_r gradually decreased. Furthermore, all samples exhibited well-defined saturation hysteresis loops, which indicated that all of the films had good ferroelectric properties. However, significant asymmetries were observed in the hysteresis loop of the BLT4 thin film, likely stemming from differences in the work function, defect charge, and interface control between the top and bottom electrodes. In Figure 3b, dielectric constant and dielectric loss are shown as functions of frequency for all thin films at room temperature. At 100 Hz, the dielectric constant increased with the film thickness, rising from 258 at 140 nm to 276 at 240 nm. The dielectric constant increases with the film thickness, influenced by both the extrinsic and intrinsic properties of the ferroelectric film. This relationship can be further elucidated. Meanwhile, the dielectric constants of all thin films decrease as the test frequency rises due to the suppression of the space charge effect. In the frequency range from 10^2 to 10^5 Hz, the dielectric loss remains nearly constant (<0.10). The abrupt changes in the dielectric constant and dielectric loss beyond 10^5 Hz result from the L-C resonance induced by the stray inductance at the probe–film contact [32].

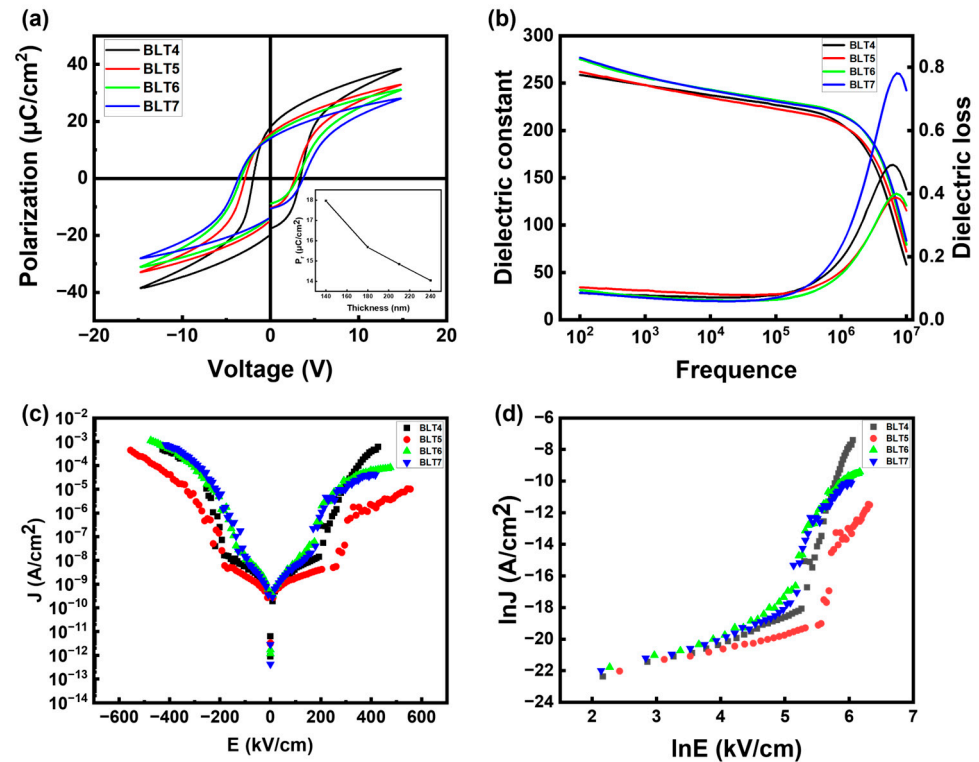


Figure 3. (a) Polarization voltage loops, (b) dielectric constant and dielectric loss as functions of frequency, (c) leakage current curves, and (d) corresponding $\ln E$ - $\ln J$ curves of BLT thin films with different film thicknesses.

It is widely recognized that BIT thin films exhibit high leakage currents, which are primarily attributed to defects like oxygen vacancies. The incorporation of La into BIT (BLT) can ameliorate the leakage current characteristics. In Figure 3c, the leakage current density versus the applied electric field (J - E) for BLT thin films with varying spin-coating times is depicted. Irrespective of the spin-coating times, all BLT thin films exhibit reduced leakage current densities, measuring less than 4.5×10^{-8} A/cm² at an electric field of 150 kV/cm. The J - E curves of all Au/BLT/Pt samples display asymmetry around $x = 0$, which is attributable to differing Schottky heights of the top and bottom electrodes in the ferroelectric heterostructures [10]. The leakage current curve manifests two distinct regions. In the low-voltage region, the leakage current densities of all BLT thin films demonstrate linear growth, while in the high-voltage region, they increase exponentially. The boundary between these two regions for BLT thin films is observed at approximately 180 kV/cm. In Figure 3d, the $\ln J$ - $\ln E$ curves for all BLT thin films illustrate a similar trend in which the current density increases with the electric field, indicating that the leakage current characteristics are independent of the film thickness. Detailed discussions on the leakage current characteristics in the low electric field and high electric field regions will be provided for the BLT4 film.

Figure 4 presents the electrical characteristics of BLT4 thin films. In Figure 4a, the hysteresis loop of the BLT4 film at 1 kHz is shown as a function of the electric field. Notably, an increase in the electric field leads to a rapid rise in both the remanent polarization and coercive field. Once the saturation voltage is reached, the coercive field remains constant, while the remanent polarization exhibits a linear increase with the electric field. In Figure 4b, we depict the frequency-dependent hysteresis loops of BLT4, revealing a decrease in maximal polarization and an increase in the corresponding remanent polarization as the frequency varies. Importantly, the hysteresis loops remain relatively stable, indicating good frequency stability. Figure 4c displays the leakage current behavior of BLT4, and the inset exhibits the $\ln J$ - $\ln E$ curve. The leakage conductance mechanism of $\ln J$ - $\ln E$ was

analyzed by the slope α of $\ln J$ - $\ln E$. In general, when $\alpha \sim 1$, the conduction mechanism is an ohmic conduction mechanism, and when $\alpha \sim 2$, the conduction mechanism is a space charge limited current mechanism (SCLC). The $\ln J$ - $\ln E$ curve of BLT4 under a positive electric field can be divided into two segments; when the electric field is low, $\alpha \sim 1.4$, this indicates that the conduction mechanism of the BLT4 film is the combined action of an ohmic conduction mechanism and an SCLC mechanism. When the electric field continues to increase, reaching $\alpha \sim 12.4$, this may be dominated by the Schottky emission mechanism and the Poole–Frenkel emission mechanism [33]. Lastly, in Figure 4d, we present the hysteresis loop of BLT4 at 8 V and its corresponding current and voltage profiles. The current-voltage curve exhibits a significant current peak near the coercive field, which is associated with ferroelectric domain inversion induced by the applied electric field. The reorientation of most domains under the applied electric field results in higher current densities, underscoring the stability of the thin film domains.

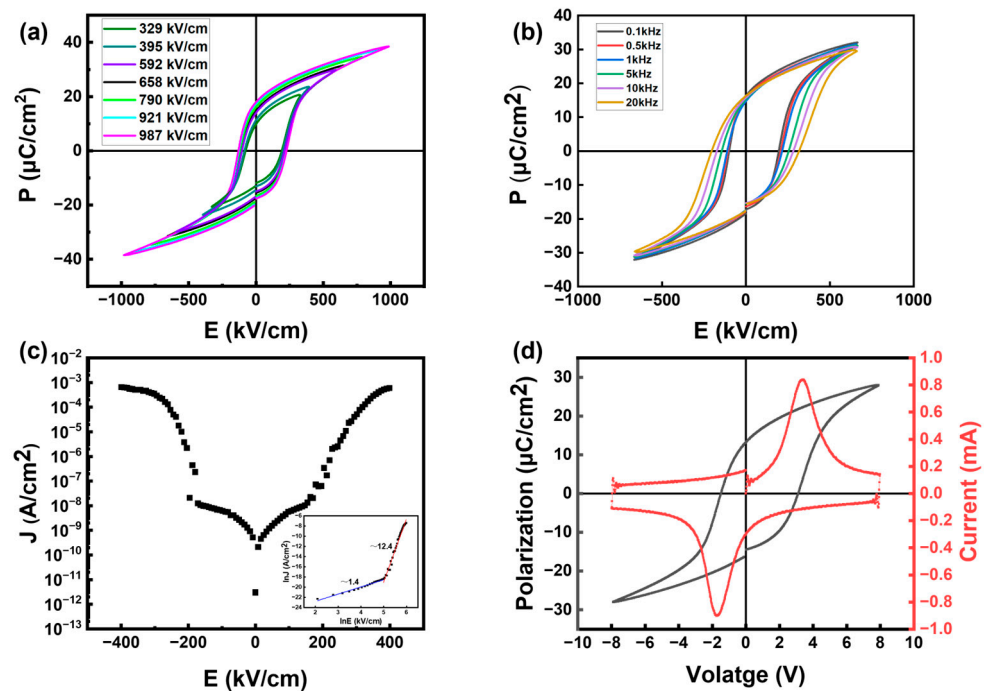


Figure 4. (a) The hysteresis loop of BLT4 of different electric fields at 1 kHz; (b) the change in BLT4 hysteresis loop with frequency; (c) the leakage current curve of BLT4; (d) the P-V hysteresis loop of BLT4 at 8 V and the corresponding I-V curve.

To confirm the presence of microscopic ferroelectricity, we utilized piezoelectric response force microscopy to examine the as-prepared BLT4 thin films in randomly selected areas. Figure 5a,b show the original amplitude and phase image of the BLT4 thin film, respectively. Figure 5c,d show the amplitude and phase image of the BLT4 thin film obtained after polarizing an area of approximately $3 \times 3 \text{ mm}^2$ at -9 V and subsequently polarizing the central region with $+9 \text{ V}$ bias. This process revealed three distinct polarization states: an outer region that remained unbiased during growth, a region biased negatively at -9 V , and a centrally biased region at $+9 \text{ V}$. These observations indicate complete polarization, switching between “up” and “down” states. Figure 5e,f show an additional PFM scan of the sample taken 30 min after the writing domain. The results indicate that the sample exhibits robust domain stability, underscoring its potential value in non-volatile ferroelectric memory applications.

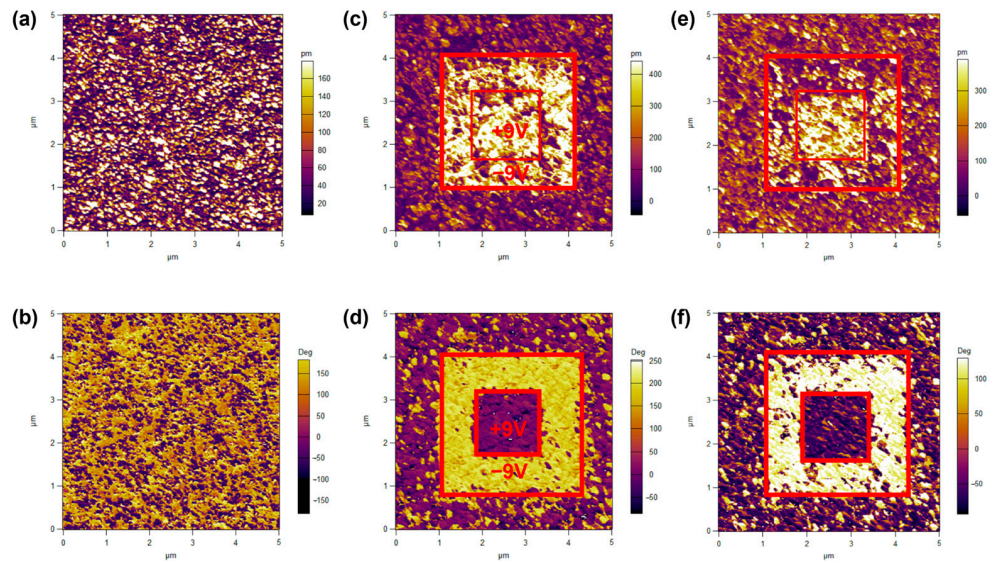


Figure 5. Out-of-plane piezoelectric force microscopy phase diagram of BLT4 film: original state (a) amplitude image, and (b) phase image; after writing domains (c) amplitude image, and (d) phase image; after 30 min (e) amplitude image, and (f) phase image.

Similarly, we conducted piezoelectric response force microscopy characterization on the as-prepared BLT5 thin films in randomly selected regions, as illustrated in Figure 6. Following domain writing, we observed that some shapes in the amplitude map matched the intended designs, yet the phase map did not exhibit clear shape features. This discrepancy arises from the fact that when writing domains, ferroelectric domains are only partially induced, which is a notable contrast to BLT4 thin films.

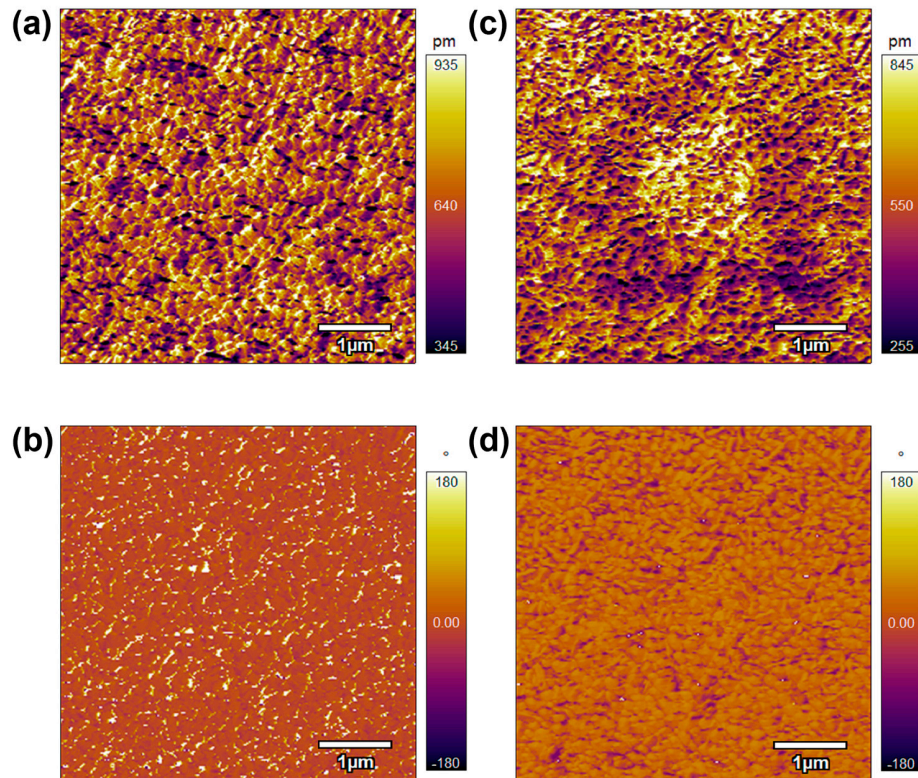


Figure 6. Out-of-plane piezoelectric force microscopy phase diagram of BLT5 film: original state (a) amplitude image, and (b) phase image; after writing domains (c) amplitude image, and (d) phase image.

To investigate the resistance characteristics of Au/BLT/Pt devices, I-V curves were measured at room temperature according to the schematic shown in Figure 7a. Figure 7b shows a semilog plot of the I-V measurement, where the arrow indicates the voltage sweep. The voltage scanning sequence is 1 → 2 → 3 → 4 → 5, and the corresponding voltage is 0 V → 6 V → 0 V → −6 V → 0 V. It can be found that the device has resistance switching characteristics. With the increase in the forward sweep voltage, an SET occurs at about 3.2 V, and the device current increases significantly. The device switches from the high-resistance state (HRS) to the low-resistance state (LRS) [34,35]. As the negative sweep voltage increases, and as the sweep voltage returns from −6 V to 0 V, the device switches from the LRS to the HRS. This shows that Au/BLT/Pt memory devices have resistor characteristics and have good application prospects in memristor.

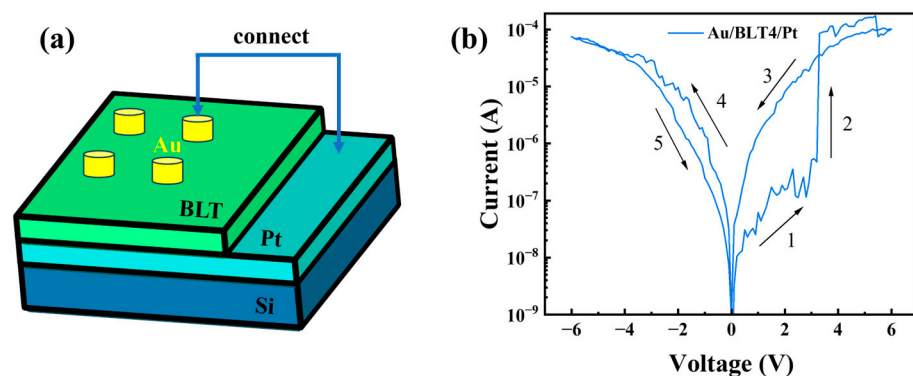


Figure 7. (a) Schematic drawing of the Au/BLT/Pt device; (b) semilogarithmic I-V curve.

4. Conclusions

In summary, $\text{Bi}_{3.25}\text{La}_{0.75}\text{Ti}_3\text{O}_{12}$ thin films were synthesized on Pt/Ti/SiO₂/Si substrates using the sol-gel method, employing various spin-coating times. All thin films show random orientations and have the appearance of rod-like grains. The findings indicate a proportional increase in the film thickness, approximately 35 nm per layer, with each additional spin-coating application. Different spin-coating durations influence the ferroelectric properties and dielectric properties of BLT thin films. The remnant polarization experienced a decrease, and the dielectric constant increased with the increased film thickness. The BLT4 thin film has a good domain flip and keeps its characteristics and resistance characteristics, which show that it has potential applications in non-volatile memory and memristors.

Author Contributions: Conceptualization, W.Y. and T.J.; methodology, W.Y., Y.C. and D.W.; software, W.Y.; validation, Y.C.; formal analysis, W.Y.; investigation, W.Y.; resources, T.J.; data curation, W.Y.; writing—original draft preparation, W.Y.; writing—review and editing, T.J. and Q.G.; visualization, Y.C.; supervision, T.J.; project administration, T.J.; funding acquisition, T.J. All authors have read and agreed to the published version of the manuscript.

Funding: This research was funded by the National Natural Science Foundation of China, grant numbers 51702351 and 51777209; the Basic and Applied Basic Research Foundation of Guangdong Province, grant number 2020B1515120019; and the Shenzhen Science and Technology Innovation Committee, grant numbers JCYJ20170413152832151 and KQTD20170810160424889.

Institutional Review Board Statement: Not applicable.

Informed Consent Statement: Not applicable.

Data Availability Statement: The data that support the finding of this study are available from the corresponding author upon reasonable request.

Conflicts of Interest: The authors declare no conflicts of interest.

References

1. Ahn, Y.; Son, J.Y. Mixed grains and orientation-dependent piezoelectricity of polycrystalline Nd-substituted $\text{Bi}_4\text{Ti}_3\text{O}_{12}$ thin films. *Ceram. Int.* **2016**, *42*, 13061–13064. [[CrossRef](#)]
2. Roy, S.; Majumder, S. Recent advances in multiferroic thin films and composites. *J. Alloy Compd.* **2012**, *538*, 153–159. [[CrossRef](#)]
3. Scott, J.F.; de Araujo, C.A.P. Ferroelectric Memories. *Science* **1989**, *246*, 1400–1405. [[CrossRef](#)] [[PubMed](#)]
4. Cheng, H.; Ouyang, J.; Zhang, Y.-X.; Ascienzo, D.; Li, Y.; Zhao, Y.-Y.; Ren, Y. Demonstration of ultra-high recyclable energy densities in domain-engineered ferroelectric films. *Nat. Commun.* **2017**, *8*, 1999. [[CrossRef](#)] [[PubMed](#)]
5. Grinberg, I.; West, D.V.; Torres, M.; Gou, G.; Stein, D.M.; Wu, L.; Chen, G.; Gallo, E.M.; Akbashev, A.R.; Davies, P.K.; et al. Perovskite oxides for visible-light-absorbing ferroelectric and photovoltaic materials. *Nature* **2013**, *503*, 509–512. [[CrossRef](#)] [[PubMed](#)]
6. Peng, G.-G.; Zheng, D.-Y.; Cheng, C.; Zhang, J.; Zhang, H. Effect of rare-earth addition on morphotropic phase boundary and relaxation behavior of the PNN-PZT ceramics. *J. Alloy Compd.* **2017**, *693*, 1250–1256. [[CrossRef](#)]
7. Kumari, S.; Ortega, N.; Pradhan, D.K.; Kumar, A.; Scott, J.F.; Katiyar, R.S. Effect of thickness on dielectric, ferroelectric, and optical properties of Ni substituted $\text{Pb}(\text{Zr}_{0.2}\text{Ti}_{0.8})\text{O}_3$ thin films. *J. Appl. Phys.* **2015**, *118*, 184103. [[CrossRef](#)]
8. Cho, S.W.; Lee, J.I.; Jeong, Y.H. Microstructure, ferroelectric and piezoelectric properties of $\text{Bi}_4\text{Ti}_3\text{O}_{12}$ platelet incorporated 0.36BiScO_3 - 0.64PbTiO_3 thick films for high temperature piezoelectric device applications. *Ceram. Int.* **2021**, *47*, 23880–23887. [[CrossRef](#)]
9. Du, X.; Huang, W.; He, S.; Kumar, T.S.; Hao, A.; Qin, N.; Bao, D. Dielectric, ferroelectric, and photoluminescent properties of Sm-doped $\text{Bi}_4\text{Ti}_3\text{O}_{12}$ thin films synthesized by sol-gel method. *Ceram. Int.* **2018**, *44*, 19402–19407. [[CrossRef](#)]
10. Ma, S.; Cheng, X.; Ma, Z.; Ali, T.; Xu, Z.; Chu, R. Effect of thickness and crystalline morphology on electrical properties of rf-magnetron sputtering deposited $\text{Bi}_4\text{Ti}_3\text{O}_{12}$ thin films. *Ceram. Int.* **2018**, *44*, 20465–20471. [[CrossRef](#)]
11. Park, B.H.; Kang, B.S.; Bu, S.D.; Noh, T.W.; Lee, J.; Jo, W. Lanthanum-substituted bismuth titanate for use in non-volatile memories. *Nature* **1999**, *401*, 682–684. [[CrossRef](#)]
12. Subbarao, E. A family of ferroelectric bismuth compounds. *J. Phys. Chem. Solids* **1962**, *23*, 665–676. [[CrossRef](#)]
13. Long, C.; Chang, Q.; Fan, H. Differences in nature of electrical conduction among $\text{Bi}_4\text{Ti}_3\text{O}_{12}$ -based ferroelectric polycrystalline ceramics. *Sci. Rep.* **2017**, *7*, 4193. [[CrossRef](#)] [[PubMed](#)]
14. Chen, Y.; Xie, S.; Wang, H.; Chen, Q.; Wang, Q.; Zhu, J.; Guan, Z. Dielectric abnormality and ferroelectric asymmetry in W/Cr co-doped $\text{Bi}_4\text{Ti}_3\text{O}_{12}$ ceramics based on the effect of defect dipoles. *J. Alloy Compd.* **2017**, *696*, 746–753. [[CrossRef](#)]
15. Roselin, A.A.; Karkuzhali, R.; Anandhan, N.; Gopu, G. Bismuth titanate ($\text{Bi}_4\text{Ti}_3\text{O}_{12}$, BTO) sol-gel spin coated thin film for heavy metal ion detection. *J. Mater. Sci. Mater. Electron.* **2021**, *32*, 24801–24811. [[CrossRef](#)]
16. Du, X.; Huang, W.; Thatikonda, S.K.; Qin, N.; Bao, D. Improved ferroelectric and dielectric properties of Sm, La co-doped $\text{Bi}_4\text{Ti}_3\text{O}_{12}$ multifunctional thin films with orange-red emission. *J. Mater. Sci. Mater. Electron.* **2019**, *30*, 13158–13166. [[CrossRef](#)]
17. Zhang, S.-T.; Chen, Z.; Zhang, C.; Yuan, G.-L. Temperature-dependent ferroelectric and dielectric properties of $\text{Bi}_{3.25}\text{La}_{0.75}\text{Ti}_3\text{O}_{12}$ thin films. *Appl. Surf. Sci.* **2010**, *256*, 2468–2473. [[CrossRef](#)]
18. Zhu, Z.; Chen, Y.-B.; Zheng, X.-J. Nanoscale domain switching mechanism of $\text{Bi}_{3.15}\text{Eu}_{0.85}\text{Ti}_3\text{O}_{12}$ thin film under the different mechanical forces. *Chin. Phys. B* **2015**, *24*, 107702. [[CrossRef](#)]
19. Zhou, H.; Wu, G.; Qin, N.; Bao, D. Dual enhancement of photoluminescence and ferroelectric polarization in $\text{Pr}^{3+}/\text{La}^{3+}$ -codoped bismuth titanate thin films. *J. Am. Ceram. Soc.* **2010**, *93*, 2109–2112. [[CrossRef](#)]
20. Wu, D.; Li, A.; Ming, N. Leakage current characteristics of Pt/ $\text{Bi}_{3.25}\text{La}_{0.75}\text{Ti}_3\text{O}_{12}$ /Pt thin-film capacitors. *J. Appl. Phys.* **2005**, *97*, 1915533. [[CrossRef](#)]
21. Kao, M.-C.; Chen, H.-Z.; Young, S.-L. The microstructure and ferroelectric properties of Sm and Ta-doped bismuth titanate ferroelectric thin films. *Thin Solid Films* **2013**, *529*, 143–146. [[CrossRef](#)]
22. Su, L.; Lu, X.; Chen, L.; Wang, Y.; Yuan, G.; Liu, J.-M. Flexible, Fatigue-Free, and Large-Scale $\text{Bi}_{3.25}\text{La}_{0.75}\text{Ti}_3\text{O}_{12}$ Ferroelectric Memories. *ACS Appl. Mater. Interfaces* **2018**, *10*, 21428–21433. [[CrossRef](#)] [[PubMed](#)]
23. Ma, S.; Cheng, X.; Ma, Z.; Xu, Z.; Chu, R. Characterization of highly (117)-oriented $\text{Bi}_{3.25}\text{La}_{0.75}\text{Ti}_3\text{O}_{12}$ thin films prepared by rf-magnetron sputtering technique. *Solid State Commun.* **2018**, *278*, 31–35. [[CrossRef](#)]
24. Xue, K.-H.; de Araujo, C.A.P.; Celinska, J. A comparative study on $\text{Bi}_4\text{Ti}_3\text{O}_{12}$ and $\text{Bi}_{3.25}\text{La}_{0.75}\text{Ti}_3\text{O}_{12}$ ferroelectric thin films derived by metal organic decomposition. *J. Appl. Phys.* **2010**, *107*, 3428968. [[CrossRef](#)]
25. Wu, A.; Soares, M.R.; Salvado, I.M.M.; Vilarinho, P.M. Sol-gel synthesis and electrical characterization of $\text{Bi}_{3.25}\text{La}_{0.75}\text{Ti}_3\text{O}_{12}$ thin films. *Mater. Res. Bull.* **2012**, *47*, 3819–3824. [[CrossRef](#)]
26. Liu, B.; Zhang, W.; Wang, Y.; Sun, H.; Li, F.; Yan, Z.; Du, J.; Zhao, Q. Impact of Pt bottom electrode on the properties of ferroelectric $\text{Bi}_{3.25}\text{La}_{0.75}\text{Ti}_3\text{O}_{12}$ capacitors. *Mater. Lett.* **2007**, *61*, 1933–1936. [[CrossRef](#)]
27. Sun, S.; Yuan, J.; Guo, W.; Duan, X.; Jia, D.; Lin, H. Thickness effects on the sinterability, microstructure, and nanohardness of SiC-based ceramics consolidated by spark plasma sintering. *J. Am. Ceram. Soc.* **2023**, *107*, 777–784. [[CrossRef](#)]
28. Zhang, W.L.; Tang, M.H.; Xiong, Y.; Wang, K.; Wang, Z.P.; Xiao, Y.G.; Yan, S.A.; Li, Z.; He, J. Influence of the annealing temperature of the $\text{Bi}_4\text{Ti}_3\text{O}_{12}$ seeding layer on the structural and electrical properties of $\text{Bi}_{3.15}\text{Nd}_{0.85}\text{Ti}_{2.99}\text{Mn}_{0.01}\text{O}_{12}$ thin films. *RSC Adv.* **2016**, *6*, 88668–88673. [[CrossRef](#)]
29. Yang, B.B.; Guo, M.Y.; Song, D.P.; Tang, X.W.; Wei, R.H.; Hu, L.; Yang, J.; Song, W.H.; Dai, J.M.; Lou, X.J.; et al. $\text{Bi}_{3.25}\text{La}_{0.75}\text{Ti}_3\text{O}_{12}$ thin film capacitors for energy storage applications. *Appl. Phys. Lett.* **2017**, *111*, 183903. [[CrossRef](#)]

30. Schwartz, R.W.; Voigt, J.A.; Tuttle, B.A.; Payne, D.A.; Reichert, T.L.; DaSalla, R.S. Comments on the effects of solution precursor characteristics and thermal processing conditions on the crystallization behavior of sol-gel derived lead zirconate titanate thin films. *J. Mater. Res.* **1997**, *12*, 444–456. [[CrossRef](#)]
31. Iljinas, A.; Stankus, V. Influence of deposition temperature on structural and ferroelectric properties of $\text{Bi}_4\text{Ti}_3\text{O}_{12}$ thin films. *Appl. Surf. Sci.* **2016**, *381*, 2–5. [[CrossRef](#)]
32. Fan, Q.; Liu, M.; Ma, C.; Wang, L.; Ren, S.; Lu, L.; Lou, X.; Jia, C.-L. Significantly enhanced energy storage density with superior thermal stability by optimizing $\text{Ba}(\text{Zr}_{0.15}\text{Ti}_{0.85})\text{O}_3/\text{Ba}(\text{Zr}_{0.35}\text{Ti}_{0.65})\text{O}_3$ multilayer structure. *Nano Energy* **2018**, *51*, 539–545. [[CrossRef](#)]
33. Zhang, W.; Gao, Y.; Kang, L.; Yuan, M.; Yang, Q.; Cheng, H.; Pan, W.; Ouyang, J. Space-charge dominated epitaxial BaTiO_3 heterostructures. *Acta Mater.* **2015**, *85*, 207–215. [[CrossRef](#)]
34. Zhou, H.-C.; Jiang, Y.-P.; Tang, X.-G.; Liu, Q.-X.; Li, W.-H.; Tang, Z.-H. Excellent Bipolar Resistive Switching Characteristics of $\text{Bi}_4\text{Ti}_3\text{O}_{12}$ Thin Films Prepared via Sol-Gel Process. *Nanomaterials* **2021**, *11*, 2705. [[CrossRef](#)]
35. Bu, Y.; Xu, T.; Geng, S.; Fan, S.; Li, Q.; Su, J. Ferroelectrics-Electret Synergetic Organic Artificial Synapses with Single-Polarity Driven Dynamic Reconfigurable Modulation. *Adv. Funct. Mater.* **2023**, *33*, 2213741. [[CrossRef](#)]

Disclaimer/Publisher’s Note: The statements, opinions and data contained in all publications are solely those of the individual author(s) and contributor(s) and not of MDPI and/or the editor(s). MDPI and/or the editor(s) disclaim responsibility for any injury to people or property resulting from any ideas, methods, instructions or products referred to in the content.